PNAS RESEARCH ARTICLE | APPLIED PHYSICAL SCIENCES

Multifractality in spin glasses

Marco Baity-Jesi[a], Enrico Calore[b], Andrés Cruz[c,d], Luis Antonio Fernández[e], José Miguel Gil-Narvión[d], Isidoro González-Adalid Pemartín[e,1], Antonio Gordillo-Guerrero[f,g], David Íñiguez[c,d,h], Andrea Maiorano[i], Enzo Marinari[j], Víctor Martín-Mayor[e], Javier Moreno-Gordo[c,d,g,k], Antonio Muñoz Sudupe[e], Denis Navarro[l], Ilaria Paga[m], Giorgio Parisi[j,1], Sergio Pérez-Gaviro[c,d], Federico Ricci-Tersenghi[j], Juan Jesús Ruiz-Lorenzo[g,k], Sebastiano Fabio Schifano[n], Beatriz Seoane[o], Alfonso Tarancón[c,d], and David Yllanes[d,p]

Contributed by Giorgio Parisi; received July 28, 2023; accepted October 21, 2023; reviewed by John Cardy and Hikaru Kawamura

We unveil the multifractal behavior of Ising spin glasses in their low-temperature phase. Using the Janus II custom-built supercomputer, the spin-glass correlation function is studied locally. Dramatic fluctuations are found when pairs of sites at the same distance are compared. The scaling of these fluctuations, as the spin-glass coherence length grows with time, is characterized through the computation of the singularity spectrum and its corresponding Legendre transform. A comparatively small number of site pairs controls the average correlation that governs the response to a magnetic field. We explain how this scenario of dramatic fluctuations (at length scales smaller than the coherence length) can be reconciled with the smooth, self-averaging behavior that has long been considered to describe spin-glass dynamics.

fractal dimensions | intermittency | disorder systems | large scale simulations

Significance

Many seemingly irregular objects (coast shores, for instance) look the same at different observation scales. In many cases, a single number, the fractal dimension, characterizes the scale changes. Other systems, known as multifractals, need a continuous range of parameters to characterize the change of scale. Multifractal behavior has been identified in a plethora of situations, from human heartbeats to financial time series, and is often accompanied by large statistical fluctuations. Spin glasses are one of the best-studied model systems for complexity, and large statistical fluctuations are completely absent from their dynamics. Our finding of multifractal scaling in the spin-glass off-equilibrium dynamics is, therefore, surprising. The paradox is solved through the concept of coherence length.

The notion of multifractality (1, 2) refers to situations where many different fractal behaviors coexist within the same system. A major role is played in this context by scale symmetry; see, e.g., (3–5): In many situations in physics, chemistry, and beyond, apparently random objects look the same when the observation scale is changed. The scale change is often quantitatively characterized through a number, the fractal dimension. Multifractals (as opposed to fractals) are systems that need many fractal dimensions to get their scaling properties fully characterized.

Some of the first examples of multifractal behavior appeared in physics, in the contexts of turbulence (6), Anderson localization (7) and diffusion-limited aggregates (8). A unifying language was soon introduced in a study of chaotic dynamics (9, 10). The concept has gained popularity as the list of systems exhibiting some form of multifractality has steadily grown. To name only a few, let us recall surface growth (11), human heartbeat dynamics (12), mating copepods (13, 14), rainfall (15), or the analysis of financial time series (16).

Here, we add a (perhaps) surprising member to the list: the off-equilibrium dynamics of spin-glass systems (17, 18). These disordered magnetic alloys have long been regarded as a paradigmatic toy model for the study of glassiness, optimization, biology, financial markets, or social dynamics. It is surprising that such a prominent feature as multifractality has gone unnoticed for such a well-studied model.*

The explanation for the above paradox rests on the finite coherence length $\xi(t_w)$ that develops when a spin glass, initially at some very high temperature, is suddenly cooled below the critical temperature T_c, and let to relax for a waiting time t_w—most experimental work on spin glasses is carried out under nonequilibrium conditions (20). As t_w increases, glassy domains of growing size $\xi(t_w)$ develop, see Fig. 1. The growth of $\xi(t_w)$ is sluggish for a spin glass, reaching only $\xi \sim 200$ lattice spacings for $t_w \sim 1$ h (21, 22). Now, when one measures the magnetic response to an external field, which is the main experimental probe of spin-glass dynamics, an average over the whole sample is carried out. Since the sample is effectively composed of many independent domains of linear size $\sim \xi(t_w)$, the central limit theorem eliminates from the average response the large fluctuations that could ultimately cause multifractal behavior. With few exceptions (see below), most numerical work has emphasized the space-averaged correlation function in Fig. 1. Besides, see *Methods*, studying correlations without spatial averages is very demanding computationally.

It follows from the above considerations that multifractal behavior in spin glasses should be investigated in large statistical deviations that occur at a length scale smaller than (or comparable to) $\xi(t_w)$, definitively not the standard framework either for experiments (see refs. 22–24, for instance) or for simulations (25–27). There is, however,

*See ref. 19 for an early, unsuccessful search of multifractality in spin glasses.

Reviewers: J.C., Center for Theoretical Physics, University of Oxford; and H.K., Molecular Photoscience Research Center, Kobe University.

The authors declare no competing interest.

[1]To whom correspondence may be addressed. Email: isidorog@ucm.es or giorgio.parisi@roma1.infn.it.

This article contains supporting information online at https://www.pnas.org/lookup/suppl/doi:10.1073/pnas.2312880120/-/DCSupplemental.

Published January 4, 2024.

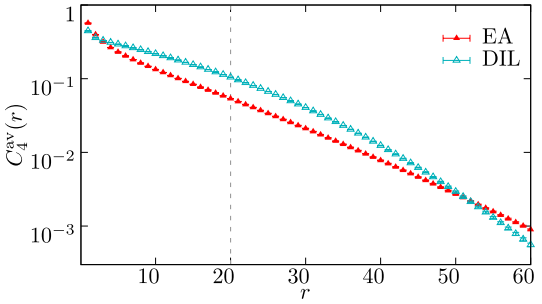

Fig. 1. The correlation function, Eq. **10**, as computed for the three-dimensional Ising diluted ferromagnet (DIL) and for the Ising spin glass (EA), versus distance r. Data were obtained in systems of linear size $L = 160$ with coherence length $\xi(t_{\rm w}) = 20$ (dashed vertical line) at temperature $T = 0.9$—recall that $T_{\rm c} \approx 1.1$ for EA (32). As explained in *Methods*, the coherence length is computed from the integral $I_2 = \int_0^\infty r^2 C_4^{\rm av}(r) {\rm d}r$ (the integrand is shown in the *SI Appendix*).

an important exception. Recently, progress has been achieved (28) in the theoretical interpretation of the experimental rejuvenation and memory effects in spin glasses (29). Crucial for this achievement was the study of temperature chaos in the off-equilibrium dynamics *at the* $\xi(t_{\rm w})$ *length scale* (30), through numerical simulations using the Janus II dedicated supercomputer (31). As we shall show below, the consideration of fluctuations at the $\xi(t_{\rm w})$ length scale still holds surprises.

Specifically, we shall consider the spin-glass correlation function, see *Methods* for definitions. The space-averaged correlation function is a well-known quantity and the basis for the computation of $\xi(t_{\rm w})$ explained in Fig. 1. We shall depart from the standard approach, however, by avoiding the spatial average. We shall compute the correlation function for a pair of sites $\boldsymbol{x}$ and $\boldsymbol{y}$, and consider the statistical fluctuations induced by varying $\boldsymbol{x}$ while fixing $\boldsymbol{r} = \boldsymbol{y} - \boldsymbol{x}$.

The reader may argue that it is difficult to find large statistical fluctuations in a mathematical object bounded between 0 and 1, such as the spin-glass correlation function. A moment of thought will reveal that large fluctuations are only possible if the average of the correlation function goes to zero as $\xi(t_{\rm w})$ grows, so that the correlation function at a given site can get large if measured in units of the averaged correlation.

Indeed, spin glasses are peculiar among systems with domain-growth off-equilibrium dynamics. Fig. 2 compares the space-averaged correlation function at distance $r = \xi(t_{\rm w})$ for two Ising systems in space dimension $D = 3$, the link-diluted ferromagnet and the spin glass. In the ferromagnet, the correlation function goes to a constant value (the squared spontaneous magnetization) as ξ grows. Hence, large deviations and multifractality are possible for the ferromagnet only at $T_{\rm c}$, where the spontaneous magnetization vanishes.[†] In the spin glass, instead, the correlation function scales as $1/r^\theta$ for distances up to $r \sim \xi$.[‡] Hence, unlike the diluted ferromagnet, the spin glass can accommodate large fluctuations for all $T < T_{\rm c}$. This is why here we decide to focus on the spin glass.

[†]At its critical temperature, the two-dimensional diluted ferromagnetic Potts model with more than two states presents multiscaling as well (33)—this is also the case for the diluted Ising model in $D = 3$ (34, 35).

[‡]The droplet picture of spin glasses (36–38) predicts $\theta = 0$, similarly to the ferromagnet. Neither simulations nor experimental data are compatible with $\theta = 0$, unless one is willing to accept that the available range of $\xi(t_{\rm w})$ is too small to display the true asymptotic behavior (27).

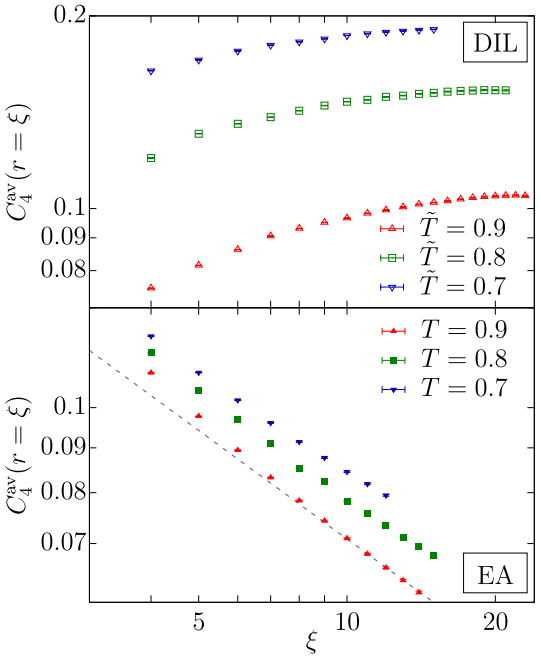

Fig. 2. Correlation function $C_4^{\rm av}(r = \xi(t_{\rm w}))$, see Eq. **10** versus the coherence length $\xi(t_{\rm w})$, as computed for DIL (*Top*) and for EA (*Bottom*) at temperatures T, $\tilde{T} = 0.9, 0.8$ and 0.7 (see *Methods* for a complete definition of $\tilde{T}$). Error bars are smaller than the point size. The dashed line is our fit to Eq. **2**, with $q = 1$, for EA at $T = 0.9$ (to avoid scaling corrections, we fit in the range $\xi(t_{\rm w}) \in [10, 20]$, see *SI Appendix* for further information). Note that, while the DIL $C_4^{\rm av}(r = \xi(t_{\rm w}))$ tends to a T-dependent positive limit for large coherence length (which excludes multiscaling at $T < T_{\rm c}$), the spin-glass correlation functions steadily decrease with $\xi(t_{\rm w})$.

Results

The first indication of large deviations in the statistics of the spin-glass correlation function C_4 is shown in Fig. 3, where we select the distance $r = \xi(t_{\rm w})$. The ratio of the second moment of C_4, $\overline{C_4^2}$, to the first moment squared, $\overline{C_4}^2$, nicely follows a power law as a function of $\overline{C_4}$ (this type of analysis was pioneered

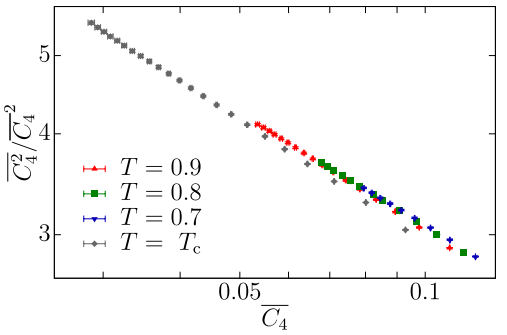

Fig. 3. Ratio of the second moment of the spin-glass correlation function C_4 computed at $r = \xi(t_{\rm w})$, $\overline{C_4^2}$, to the squared first moment, $\overline{C_4}^2$, as a function of $\overline{C_4}$. We show the data for all temperatures considered in this work. $\overline{C_4}$ tends to zero as the coherence length $\xi(t_{\rm w})$ gets large, recall Fig. 2. Note that $\overline{C_4^2}/\overline{C_4}^2$ scales with $\overline{C_4}$ as a power law, which indicates that in the scaling limit (*i.e.*, $\xi(t_{\rm w}) \to \infty$ or $\overline{C_4} \to 0$) the order of magnitude of $\overline{C_4^2}$ is larger than the one of $\overline{C_4}^2$. Data in the glassy phase, $T < T_{\rm c}$, roughly follow the same scaling curve. At the critical point, there is still a power type relation with a slightly different exponent. Error bars are smaller than the points size. The same data are shown as a function of $\xi(t_{\rm w})$ in *SI Appendix*.

in ref. 39). If continued to $\overline{C_4} \to 0$ (i.e., as $\xi(t_w)$ grows, see Fig. 2), this power law implies that the orders of magnitude of $\overline{C_4^2}$ and $\overline{C_4}^2$ differ in the large-$\xi(t_w)$ scaling limit. This behavior is not reminiscent of a monofractal, which in the scaling limit is characterized by a single quantity (say, $\overline{C_4}$).

We also note from Fig. 3 that all our data with $T < T_c$ follow the same scaling curve, which slightly differs from its counterpart at the critical point. This is not completely unexpected, because the ϵ-expansion tells us that the average C_4 at T_c decays as a power law with distance with an exponent (40) that is twice as large as the exponent for $T < T_c$ (41). In fact, we lack an explanation for the similarity of the two exponents that can be observed in Fig. 3. From now on, our analysis will focus on our data at $T = 0.9$, namely the temperature in the spin-glass phase where we are able to reach the largest $\xi(t_w)$.

A picture of the physical situation is presented in Fig. 4. We may expect a different behavior for the average and the local correlation function when distances up to $r \sim \xi(t_w)$ are considered [$\theta(T = 0.9) \approx 0.4$ (27)]:[§]

$$C_4^{\rm av}(r, t_w) \sim \frac{1}{r^\theta}, \quad C_4(\boldsymbol{x}, \boldsymbol{x}+\boldsymbol{r}; t_w) \sim \frac{1}{r^{\theta M(\boldsymbol{x},\boldsymbol{r},t_w)}}. \qquad [1]$$

As the reader can check from Fig. 4, the order-of-magnitude modulating factor $M(\boldsymbol{x}, \boldsymbol{r}, t_w)$ varies by a factor of 16, which indicates that there are site pairs $(\boldsymbol{x}, \boldsymbol{x}+\boldsymbol{r})$ a lot more —or a lot less— correlated than the average. In fact, see Fig. 5, the median correlation function at distance $r = \xi(t_w)$, scales as $[C_4^{\rm av}]^a$, with $a \approx 1.5$. In other words, the typical correlation function is a lot smaller than the average value.

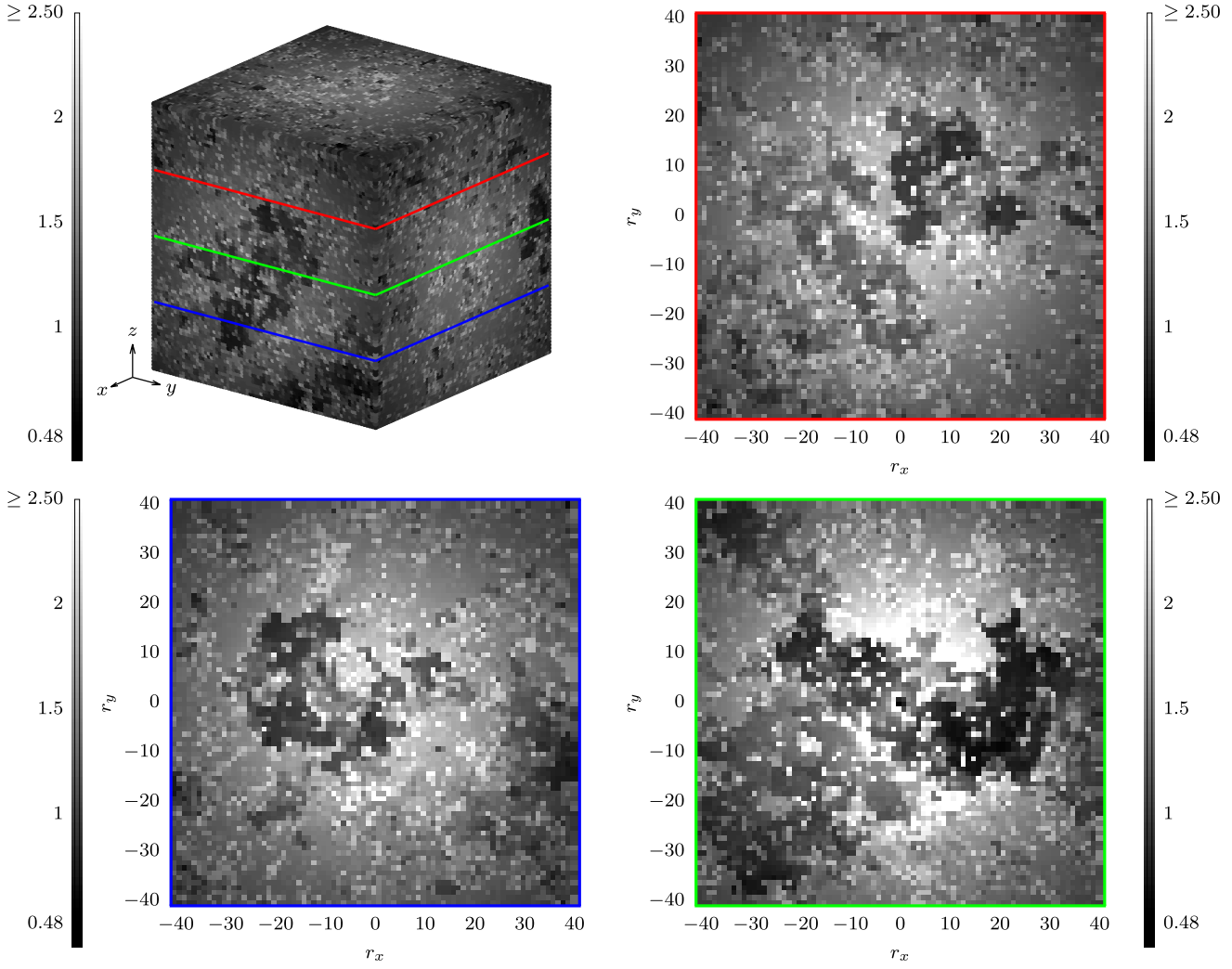

Fig. 4. Grayscale representation of the order-of-magnitude modulating factor $M(\boldsymbol{x}, \boldsymbol{r}, t_w)$, see Eq. **1**, computed for site $\boldsymbol{x} = (64, 64, 64)$ of a sample with coherence length $\xi(t_w) = 20$, at $T = 0.9$, with an $N_R = 512$ estimator (*Methods*). We show results for displacement vectors $\boldsymbol{r} = (r_x, r_y, r_z)$ in a cube $-40 \le r_x, r_y, r_z \le 40$. The *Top-Left* panel depicts the three visible faces of the cube, while the other three panels show sections at $r_z = -20, 0, 20$, respectively. Our color code is darker the smaller $M(\boldsymbol{x}, \boldsymbol{r}, t_w)$ (hence, the more slowly correlations decay with distance). For ease of representation, we have chosen a color code linear between the minimal value of $M(\boldsymbol{x}, \boldsymbol{r}, t_w)$ and 2.5. Displacements $\boldsymbol{r}$ with $M(\boldsymbol{x}, \boldsymbol{r}, t_w) > 2.5$ are depicted as if $M(\boldsymbol{x}, \boldsymbol{r}, t_w) = 2.5$. See *SI Appendix* for more examples of this modulating factor.

[§]The correlation function behaves as $C_4^{\rm av}(r, t_w) \sim G(r/\xi(t_w))/r^\theta$ for large r, where the cut-off function $G(x)$ decays faster than exponentially as x grows [see, e.g., refs. 42 and 43]. Hence, for $r \sim \xi(t_w)$ one may consider either power-law scaling in r—as in Eq. **1**—or in $\xi(t_w)$—as in Eq. **2**. The analysis of scale invariance in a fractal (or multifractal) geometry typically involves power laws.

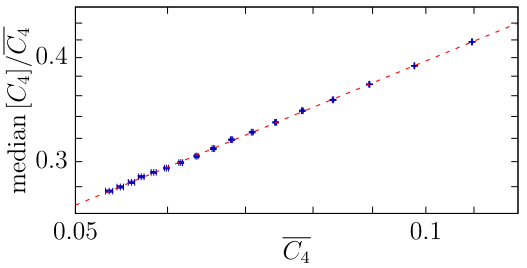

Fig. 5. Median of the distribution $P[C_4(r=\xi)]$ in units of the first moment, $\overline{C_4}(r=\xi)$, versus $\overline{C_4}(r=\xi)$, as computed for the spin glass at temperature $T=0.9$. We show data in the logarithmic scale. Therefore, the dashed line (a power-law fit with exponent ~ 0.5, see *SI Appendix* for details) appears as a straight line.

In order to make the above qualitative description quantitative, we consider the moments of the probability distribution of C_4 at distance $r=\xi(t_w)$. The q-th moment turns out to follow a scaling law

$$\overline{C_4^q} \sim \frac{A_q}{\xi^{\tau(q)}}\,. \qquad [2]$$

Fig. 6 shows the $\tau(q)$ function, which significantly differs from the monofractal behavior $\tau^{\rm mono}(q) = q\,\tau^{\rm mono}(1)$. It is this departure from linear behavior that justifies using the term *multifractal* to describe spin-glass dynamics (see, e.g., ref. 9).

For large moments, $\tau(q)$ seems to grow as $\log q$ (see the *Inset* in Fig. 6). The origin of this logarithmic growth seems to be in the behavior of the probability distribution function $P(C_4)$ near $C_4=1$. As shown in *SI Appendix*, the numerical data are consistent with $P(C_4)\propto(1-C_4)^{B(\xi)}$ for C_4 close to 1, with an exponent that grows as $B(\xi(t_w))\sim\log\xi(t_w)$. This behavior of the correlation function would explain the observed logarithmic growth of $\tau(q)$. However, just to be on the safe side, we have tried two different functional forms to fit the numerical data in Fig. 6:

$$\tau_1(q) = mq\frac{1+c_1 q}{1+c_2 q}\,,\quad \tau_2(q) = mq\frac{1+d_1 q\log q}{(1+d_2 q)^2}\,. \qquad [3]$$

Both τ_1 and τ_2 have the same derivative m at $q=0$. We do not treat m as a fitting parameter. Rather, we take it from the scaling of the *median* of the distribution $P(C_4)$ with ξ (*SI Appendix*). Although both $\tau_1(q)$ and $\tau_2(q)$ make an excellent job at fitting our data (see again *SI Appendix*), only $\tau_2(q)$ displays the logarithmic growth with q, at large q, that we find more plausible.

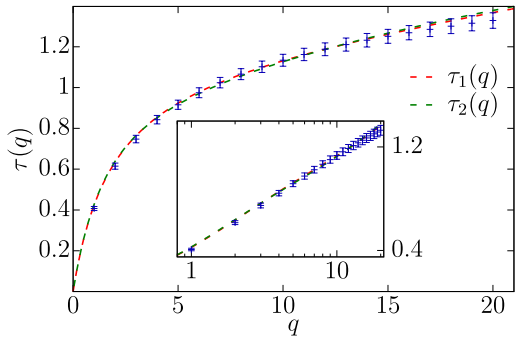

Fig. 6. Scaling exponent $\tau(q)$ for the q-th moment $\overline{C_4(r=\xi)^q}\sim\xi^{-\tau(q)}$ computed from simulations of the Ising spin glass at $T=0.9$ (see *SI Appendix* for results at T_c). The nonlinear behavior is a strong indication of multifractality. The dashed lines are fits to the functional forms in Eq. **3** (the goodness-of-fit statistics are presented in the *SI Appendix*). The *inset* presents the same data as a function of $\log(q)$.

Discussion

Following ref. 9, we shall discuss our results in terms of a different stochastic variable, $\alpha = \log C_4(r=\xi(t_w))/\log[1/\xi(t_w)]$, so that (we drop the argument in ξ for the sake of shortness)

$$C_4 = \frac{1}{\xi^\alpha}\,,\quad P(C_4)\frac{{\rm d}C_4}{{\rm d}\alpha}\sim\xi^{f(\alpha)}\,. \qquad [4]$$

Eq. **4** defines the large-deviations function $f(\alpha)$. Then, we find for the moments of C_4

$$\overline{C_4^q} = \int_0^1 {\rm d}C_4\,P(C_4)C_4^q \sim \int_0^\infty {\rm d}\alpha\,{\rm e}^{\log(\xi)[f(\alpha)-q\alpha]}\,. \qquad [5]$$

For large ξ, the above integral is dominated by the maximum of $[f(\alpha)-q\alpha]$ at some value $\alpha=\alpha^*$:

$$\overline{C_4^q} \sim \frac{1}{\xi^{-[f(\alpha^*)-q\alpha^*]}}\,. \qquad [6]$$

Comparing with Eq. **2**, we realize that $f(\alpha)$ is just (minus) the Legendre transform of the singularity spectrum $\tau(q)$:

$$f(\alpha) = -\max_q\left[\tau(q)\,-\,q\alpha\right]. \qquad [7]$$

We show $f(\alpha)$ in Fig. 7, as computed from our fitting ansätze $\tau_1(q)$ and $\tau_2(q)$, in Eq. **3**. In the range of Fig. 6—since $\alpha(q)=\tau'(q)$—the results from the two ansätze can hardly be distinguished. The two, however, differ in that the range of α for $\tau_2(q)$ goes all the way down to $\alpha=0$ (because $\alpha_2(q)={\rm d}\tau_2/{\rm d}q\sim 1/q$). Indeed, if $\tau(q)$ goes as $\log(q)$ for large q, then the large-deviations function goes as $f(\alpha\to 0)\sim\log(\alpha)$.

Let us recapitulate: the probability of finding a site $\boldsymbol{x}$ with $C_4(\boldsymbol{x},\boldsymbol{x}+\boldsymbol{r})$ scaling as $1/r^\alpha$ for $r\sim\xi$ goes in the scaling limit as $\xi^{f(\alpha)}$. There are, hence, a lot more sites displaying the median scaling exponent $\alpha\approx 0.65$ than there are for the average scaling $\alpha\approx 0.4$ (because $f(0.65)>f(0.4)$, recall Fig. 5). The larger $\xi(t_w)$ grows, the more pronounced this difference is. Thus, the expression "silent majority" (44) could be aptly employed to

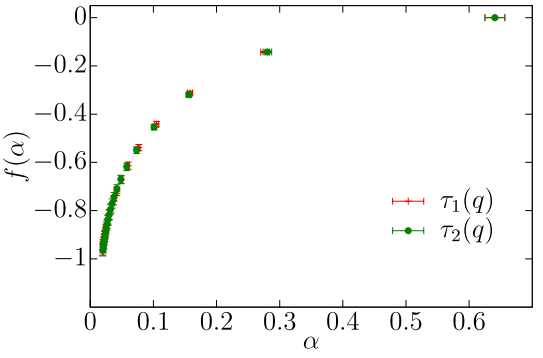

Fig. 7. Legendre transformation $f(\alpha)$ of function $\tau(q)$, see Eq. **7**, as a function $\alpha={\rm d}\tau/{\rm d}q$, computed from the fitting ansätze in Eq. **3**. Errors on both axes have been obtained as explained in *Methods* (for further details, see ref. 50). Since $f(\alpha)$ is the large-deviations function of the decay rate $C_4(r=\xi)\sim r^{-\alpha}$, the data show that the majority of sites have the median decay rate of approximately 0.65, much larger than the mean decay rate $\alpha\approx 0.4$.

describe spin-glass dynamics: the central limit theorem ensures that it is the (somewhat exceptional) average value the one that can be measured on length scales larger than $\xi(t_w)$ (hence, in experiments). The experimental-scale dynamics is, however, not completely blind to these short-scale fluctuations. Indeed, temperature chaos (30)—and, hence, rejuvenation (28), which is certainly experimentally observable (see, e.g., ref. 29)—is ruled by statistical fluctuations at the scale of r smaller than, or similar to, $\xi(t_w)$.

Our data show that varying T simply changes $\tau(q)$ by an essentially constant factor [e.g., $\tau(q, T_c) \approx 1.5\tau(q, T = 0.9)$, see *SI Appendix*]. Furthermore, Fig. 3 makes us confident that, taking $\overline{C_4}$ as scaling variable instead of $\xi(t_w)$, the overall picture is essentially temperature independent for $T < T_c$.

Whether or not multifractal behavior is also present in equilibrium correlation functions in the spin-glass phase stands out as an interesting open question. Statics-dynamics equivalence (26, 45–47) suggests that the answer will be positive.

As a final remark, let us stress that ongoing efforts to build a mathematically rigorous theory of nonequilibrium spin-glass dynamics through the concept of the maturation metastate (see ref. 48 and references therein) should take into account the extreme spatial heterogeneity unveiled in this work.

Materials and Methods

Model and Simulations. We focus on the Edwards–Anderson model (EA) in a simple cubic lattice with linear size $L = 160$ and periodic boundary conditions. Our $S_{\boldsymbol{x}} = \pm 1$ spin, placed at the lattice sites, interact with their nearest neighbors through the Hamiltonian:

$$\mathcal{H} = -\sum_{\langle \boldsymbol{x},\boldsymbol{y}\rangle} J_{\boldsymbol{x},\boldsymbol{y}} S_{\boldsymbol{x}} S_{\boldsymbol{y}} \,. \qquad [8]$$

The coupling constants $J_{\boldsymbol{x},\boldsymbol{y}}$ are independent random variables ($J_{\boldsymbol{x},\boldsymbol{y}} = \pm 1$ with equal probability), fixed once and for all at the beginning of the simulation (this is named quenched disorder). A realization of the couplings is called a *sample*. We shall use 16 samples in this work. In general, errors will be computed with a jackknife method over the samples (see, for instance, refs. 49 and 50). We have also considered a diluted Ising model (see below), as a baseline model displaying domain-growth off-equilibrium dynamics.

We have simulated the model in Eq. **8** through a Metropolis dynamics on the Janus II supercomputer (31). Our time unit is a full-lattice sweep, roughly equivalent to a picosecond of physical time (17). The critical temperature for this model is $T_c = 1.1019(29)$ (32).

For each sample, we have simulated $N_R = 512$ statistically independent system copies or *replicas*. We denote by $\langle \cdots \rangle$ the average over thermal noise for one sample (as explained below, we obtain unbiased estimators of the thermal expectation values $\langle \cdots \rangle$ by averaging over the replicas). The subsequent average over samples is denoted by an overline ($\overline{\langle \cdots \rangle}$).

The main quantity of interest is the correlation function

$$C_4(\boldsymbol{x}, \boldsymbol{y}, t_w) = \langle S_{\boldsymbol{x}}(t_w) S_{\boldsymbol{y}}(t_w)\rangle^2 \,. \qquad [9]$$

Note that, for a given sample and $(\boldsymbol{x}, \boldsymbol{y}, t_w)$, $C_4(\boldsymbol{x}, \boldsymbol{y}, t_w)$ is not a stochastic variable. However, it *is* a stochastic variable if we regard the variations induced by the choice of couplings $J_{\boldsymbol{x},\boldsymbol{y}}$ and over the considered sites $(\boldsymbol{x}, \boldsymbol{y}, t_w)$. We term these stochastic variables C_4, without arguments.

As explained in the next paragraph, although $C_4(\boldsymbol{x}, \boldsymbol{y}, t_w)$ cannot be computed with a finite number of replicas, unbiased estimators of its moments can be computed. In particular, previous work has mostly focused on the average correlation function

$$C_4^{\text{av}}(\boldsymbol{r}, t_w) = \frac{1}{L^3} \sum_{\boldsymbol{x}} \overline{C_4(\boldsymbol{x}, \boldsymbol{y} = \boldsymbol{x} + \boldsymbol{r}, t_w)} \,. \qquad [10]$$

Table 1. Maximum t_w and coherence length reached for each of our models and simulation temperatures

T or $\tilde{T}$	t_w(EA)	ξ_{max}(EA)	t_w(DIL)	ξ_{max}(DIL)
0.7	46,531,866,276	12	498	15
0.8	18,734,780,191	15	919	21
0.9	15,172,184,825	20	954	23

Cubic symmetry, present in averages over the samples, allows us to average over the three equivalent displacements $\boldsymbol{r} = (r, 0, 0)$ and permutations. We shall use the shorthand $C_4^{\text{av}}(r, t_w)$ to indicate this average over the three equivalent $\boldsymbol{r}$. To compute the coherence length $\xi(t_w)$, we follow (27, 42, 51) and compute the integrals

$$I_n(t_w) = \int_0^\infty r^n \, C_4^{\text{av}}(r, t_w) \mathrm{d}r \,. \qquad [11]$$

Then, $\xi(t_w) = I_2(t_w)/I_1(t_w)$.

As stated above, we have simulated, as a null experiment, the link-diluted Ising model (DIL). The only difference with the Hamiltonian in Eq. **8** is in the choice of the couplings: $J_{\boldsymbol{x},\boldsymbol{y}} = 1$ (with 70% probability) or $J_{\boldsymbol{x},\boldsymbol{y}} = 0$ (with 30% probability). Since all couplings are positive or zero, this is a ferromagnetic system without frustration. All our simulation and analysis procedures are identical for the DIL and EA models. The critical temperature is $T_c^{\text{DIL}} = 3.0609(5)$ (52). Actually, this is twice the value reported in ref. 52 due to our use of an Ising, rather than Potts, formulation. In fact, with some abuse of language, in the main text, we refer to DIL temperatures as $\tilde{T} = 0.9$, $\tilde{T} = 0.8$ or 0.7 rather than to their real value $T^{\text{DIL}} = \tilde{T}\,(T_c^{\text{DIL}}/T_c^{\text{EA}})$.

The range of coherence length and simulation times in this study can be found in Table 1.

Unbiased Estimators of Powers of $C_4(\boldsymbol{x}, \boldsymbol{y}, t_w)$. Given $\boldsymbol{x}$ and $\boldsymbol{y}$, we need an unbiased estimator of $C_4^q(\boldsymbol{x}, \boldsymbol{y}, t_w) = \langle S_{\boldsymbol{x}}(t_w) S_{\boldsymbol{y}}(t_w)\rangle^{2q}$. Note that the $q = 1$ instance is needed to evaluate Eq. **10**.

Should we have (at least) $2q$ replicas at our disposal, a tentative solution would be provided by the estimator

$$[C_4(\boldsymbol{x}, \boldsymbol{y}, t_w)]_q^{\text{poor}} = \prod_{a=1}^{2q} S_{\boldsymbol{x}}^{(a)}(t_w) S_{\boldsymbol{y}}^{(a)}(t_w) \,. \qquad [12]$$

$[C_4(\boldsymbol{x}, \boldsymbol{y}, t_w)]_q^{\text{poor}} = (-1)^p$, where p is the number of replicas for which $S_{\boldsymbol{x}}^{(a)}(t_w) S_{\boldsymbol{y}}^{(a)}(t_w) = -1$. However, the statistical independence of the different replicas ensures for the expectation value $\langle [C_4(\boldsymbol{x}, \boldsymbol{y}, t_w)]_q^{\text{poor}}\rangle = \langle S_{\boldsymbol{x}}(t_w) S_{\boldsymbol{y}}(t_w)\rangle^{2q}$.

Nevertheless, if we have at our disposal a number of replicas $N_R \gg 2q$, as is our case, the solution in Eq. **12** is very unsatisfactory. Rather, one would like to consider all possible picks of $2q$ *different* replicas (out of the N_R possible choices), compute $[C_4(\boldsymbol{x}, \boldsymbol{y}, t_w)]_q^{\text{poor}}$ for every pick, and take the average of those products.

To achieve our goal, we have solved the following auxiliary combinatorial problem. Given a set of N_R different signs $c_a = \pm 1$, M of which negative, we have computed $\tilde{P}(N_R, M; S, p)$, namely the probability of getting p negative signs in a pick (with uniform probability) of S *distinct* signs. With this probability in our hands, the solution is straightforward. We just need to look at our set $S_{\boldsymbol{x}}^{(a)}(t_w) S_{\boldsymbol{y}}^{(a)}(t_w)$, $a = 1, 2 \ldots, N_R$, count the number M of them that turn out to be negative and compute the estimator

$$[C_4(\boldsymbol{x}, \boldsymbol{y}, t_w)]_q = G(N_R, M, q) \,, \qquad [13]$$

$$G(N_R, M, q) = \sum_{p=0}^{2q} (-1)^p \, \tilde{P}(N_R, M; S = 2q, p) \,. \qquad [14]$$

$[C_4(\boldsymbol{x}, \boldsymbol{y}, t_w)]_q$ is an unbiased estimator of $\langle S_{\boldsymbol{x}}(t_w) S_{\boldsymbol{y}}(t_w)\rangle^{2q}$, because it is an average over all possible (poor, but unbiased) estimators in Eq. **12**. Our computation of $\tilde{P}(N_R, M; S = 2q, p)$ is explained in the *SI Appendix*.

The Probability Distribution of the Correlation Function. We wish to study the probability distribution function (pdf) for $\langle S_{\boldsymbol{x}}(t_w) S_{\boldsymbol{x}+\boldsymbol{r}}(t_w)\rangle^2$ (periodic boundary conditions are assumed for $\boldsymbol{x} + \boldsymbol{r}$). We have only considered displacements $\boldsymbol{r} = (r, 0, 0)$ –and permutations– and we have chosen the measuring times in such a way that $r = \xi(t_w)$.

Note that, given the starting point $\boldsymbol{x}$ and the sample $\{J_{\boldsymbol{x},\boldsymbol{y}}\}$, $\langle S_{\boldsymbol{x}} S_{\boldsymbol{x}+\boldsymbol{r}}\rangle^2$ is not a fluctuating quantity. Hence, we are referring to the pdf as $\boldsymbol{x}$ and the sample vary. $\langle S_{\boldsymbol{x}} S_{\boldsymbol{x}+\boldsymbol{r}}\rangle^2$ can be computed exactly only in the limit $N_R \to \infty$. However, as explained in the previous paragraph, we can compute without bias its q-th moment provided that the number of replicas at our disposal is $N_R \geq 2q$.

The basic object we compute from our simulation is the pdf $\mathcal{P}(M; N_R, \xi)$, namely the probability, as computed over the starting point $\boldsymbol{x}$ and the samples, that exactly M of the N_R signs $S^{(a)}_{\boldsymbol{x}}(t_w) S^{(a)}_{\boldsymbol{x}+\boldsymbol{r}}(t_w)$ turn out to be -1 in our simulation of this specific sample. Hence, the unbiased estimator of the q-th moment of $\langle S_{\boldsymbol{x}}(t_w) S_{\boldsymbol{x}+\boldsymbol{r}(t_w)}\rangle^2$ with $r = \xi(t_w)$ is

$$\overline{C_4^q}(\xi) = \sum_{M=0}^{N_R} \mathcal{P}(M; N_R, \xi) G(N_R, M, q)\,, \qquad [15]$$

where $G(N_R, M, q)$ was defined in Eq. **14**.

Unfortunately, the median of the pdf for $\langle S_{\boldsymbol{x}}(t_w) S_{\boldsymbol{x}+\boldsymbol{r}}(t_w)\rangle^2$ is more difficult to compute. Our strategy, explained in full detail in *SI Appendix*, consists in computing biased estimators of the median, with bias of order $1/N_R$. Then we compute these biased estimators for a sequence $N_R{}' = 32, 64, 128, 256$ and 512, and proceed to an extrapolation $N_R \to \infty$. We obtain the $\mathcal{P}(M'; N_R{}', \xi)$ from their $N_R = 512$ counterpart as

$$\mathcal{P}(M'; N_R{}', \xi) = \sum_{M=0}^{N_R} \mathcal{P}(M; N_R, \xi)\, P(N_R, M; S = N_R{}', p = M')\,. \qquad [16]$$

The probabilities $P(N_R, M; S, p)$ were defined in the previous subsection in this *Methods* section.

Computation of $\tau(q)$. In order to minimize corrections to scaling, we have fitted the normalized moments as

$$\frac{\overline{C_4^q}}{\overline{C_4}^q} = \left[\frac{A_q}{\overline{C_4}}\right]^{\beta(q)}, \quad \tau(q) = \tau(1)[q - \beta(q)]\,. \qquad [17]$$

Fig. 3 provides an example. In order to obtain good fits, we have needed to discard (at most) one data point corresponding to the smallest $\xi(t_w)$. An advantage of this method is that we only need to consider the $\xi(t_w)$ dependence to obtain $\tau(1)$, as shown in Fig. 2. The full procedure is illustrated in *SI Appendix*.

To compute errors, we have followed the strategy of ref. 50, namely carrying out all fits separately for each jackknife block (when minimizing χ^2 to perform the fits, we only consider the diagonal elements of the covariance matrix). Errors in the fit parameters are obtained from the fluctuations of the jackknife blocks.

Computation of $M(\boldsymbol{x}, r)$. The order-of-magnitude factor in Eq. **1** is computed as $\log|[C_4(\boldsymbol{x}, \boldsymbol{x}+\boldsymbol{r}, t_w)]_1|/\log C_4^{\rm av}(\sqrt{r_x^2 + r_y^2 + r_z^2})$, where $[C_4(\boldsymbol{x}, \boldsymbol{x}+\boldsymbol{r}, t_w)]_1$ is the $q = 1$ estimator in Eq. **13** (as computed with $N_R = 512$). $C_4^{\rm av}(r)$ is interpolated to noninteger arguments using a fit obtained from data with integer r (*SI Appendix*).

Data, Materials, and Software Availability. All study data are included in the article and/or *SI Appendix*. The data and the scripts that generate the figures in the main text can be downloaded from https://github.com/JanusCollaboration/multifractal_EA/tree/main/MAIN (53). The data and the scripts that generate the figures in the *SI Appendix* can be downloaded from https://github.com/JanusCollaboration/multifractal_EA/tree/main/SI (54).

ACKNOWLEDGMENTS. We thank Roberto Benzi and Luca Biferale for relevant discussions. This work was supported in part by Grants Nos. PID2022-136374NB-C21, PID2022-136374NB-C22, PID2020-112936GB-I00, PID2019-103939RB-I00, PGC2018-094684-B-C21, PGC2018-094684-B-C22, and PID2021-125506NA-I00, funded by MCIN/AEI/10.13039/501100011033 by "ERDF A way of making Europe" and by the European Union. E.M. acknowledges funding from the Progetti di Rilevante Interesse Nazionale (PRIN) funding scheme (2022LMHTET–Complexity, disorder and fluctuations: spin glass physics and beyond) and from the FIS (Fondo Italiano per la Scienza) funding scheme (FIS783–SMaC–Statistical Mechanics and Complexity: theory meets experiments in spin glasses and neural networks) from Italian Ministry of University and Research. The research has also received financial support from the Simons Foundation (Grant No. 454949, G.P.) and Italian Research Center on High Performance Computing, Big Data and Quantum Computing, funded by European Union–NextGenerationEU. DY was supported by the Chan Zuckerberg Biohub. I.G.-A.P. was supported by the Ministerio de Ciencia, Innovación y Universidades (Spain) through Formación del Profesorado Universitario (FPU) Grant No. FPU18/02665. J.M.G.-N. was supported by the Ministerio de Universidades and the European Union NextGeneration EU/PRTR through 2021–2023 Margarita Salas grant. I.P. was supported by LazioInnova-Regione Lazio under the program Gruppi di ricerca2020–POR FESR Lazio 2014-2020, Project NanoProbe (Application code A0375-2020-36761).

Author affiliations: [a]Eawag, CH-8600 Dübendorf, Switzerland; [b]Dipartimento di Fisica e Scienze della Terra, Università di Ferrara and INFN, 44122 Ferrara, Italy; [c]Departamento de Física Teórica, Universidad de Zaragoza, 50009 Zaragoza, Spain; [d]Instituto de Biocomputacíon y Física de Sistemas Complejos (BIFI), 50018 Zaragoza, Spain; [e]Departamento de Física Teórica, Universidad Complutense, 28040 Madrid, Spain; [f]Departamento de Ingeniería Eléctrica, Electrónica y Automática, Universidad de Extremadura, 10003 Cáceres, Spain; [g]Instituto de Computacíon Científica Avanzada (ICCAEx), Universidad de Extremadura, 06006 Badajoz, Spain; [h]Fundación Agencia Aragonesa para la Investigación y el Desarrollo (ARAID), Diputacíon General de Aragón, 50018 Zaragoza, Spain; [i]Dipartimento di Biotecnologie, Chimica e Farmacia, Universitá degli studi di Siena, 3100 Siena and Istituto Nazionale di Fisica Nucleare (INFN), 00185 Rome, Italy; [j]Dipartimento di Fisica, Sapienza Università di Roma, and Consiglio Nazionale delle Ricerche-Nanotec, Rome Unit and Istituto Nazionale di Fisica Nucleare (INFN), 00185 Rome, Italy; [k]Departamento de Física, Universidad de Extremadura, 06006 Badajoz, Spain; [l]Departamento de Ingeniería, Electrónica y Comunicaciones and Instituto de Investigación en Ingeniería de Aragón (I3A), Universidad de Zaragoza, 50018 Zaragoza, Spain; [m]Institute of Nanotechnology, Consiglio Nazionale delle Ricerche, I-00185 Rome, Italy; [n]Dipartimento di Scienze dell'Ambiente e della Prevenzione, Universitá di Ferrara e INFN Sezione di Ferrara, I-44122 Ferrara, Italy; [o]Université Paris-Saclay, CNRS, Institut National de Recherche en Informatique et en Automatique (INRIA) Tau team, Laboratoire Interdisciplinaire des Sciences du Numérique (LISN), 91190, Gif-sur-Yvette, France; and [p]Chan Zuckerberg Biohub, San Francisco, CA 94158

Author contributions: L.A.F., I.G.-A.P., V.M.-M., and G.P. designed research; I.G.-A.P. performed research; M.B.-J., E.C., A.C., J.M.G.-N., A.G.-G., D.Í., A.M., J.M.-G., A.M.S., D.N., S.P.-G., S.F.S., B.S., and A.T. contributed new reagents/analytic tools; L.A.F., I.G.-A.P., E.M., V.M.-M., I.P., G.P., F.R.-T., J.J.R.-L., and D.Y. analyzed data; M.B.-J., E.C., A.C., L.A.F., I.G.-A.P., A.G.-G., A.M., V.M.-M., J.M.-G., A.M.S., I.P., S.P.-G., S.F.S., and B.S. janus II hardware and software development; J.M.G.-N. janus II/Janus simulation software, Janus II hardware and software development; D.Í. and A.T. design of the Janus II project, Janus II hardware and software development; D.N. janus II/Janus simulation software; and I.G.-A.P. and V.M.-M. wrote the paper.

1. U. Frisch, G. Parisi, "On the singularity structure of fully developed turbulence" in *Turbulence and Predictability in Geophysical Fluid Dynamics and Climate Dynamics (1983 International School of Physics "Enrico Fermi", Varenna)*, M. Ghil, R. Benzi, G. Parisi, Eds. (North-Holland, Amsterdam, 1985).
2. D. Harte, *Multifractals. Theory and Applications* (Chapman and Hall/CRC, New York, NY, ed. 1, 2001).
3. K. G. Wilson, Problems in Physics with many Scales of Length. *Sci. Am.* **241**, 158–179 (1979).
4. G. Parisi, *Statistical Field Theory* (Addison-Wesley, 1988).
5. M. Barnsley, *Fractals Everywhere* (Dover Publications, Inc., Mineola, NY, ed. 3, 2012).
6. R. Benzi, G. Paladin, G. Parisi, A. Vulpiani, On the multifractal nature of fully developed turbulence and chaotic systems. *J. Phys. A: Math. General* **17**, 3521 (1984).
7. C. Castellani, L. Peliti, Multifractal wavefunction at the localisation threshold. *J. Phys. A: Math. General* **19**, L429 (1986).
8. H. E. Stanley, P. Meakin, Multifractal phenomena in physics and chemistry. *Nature* **335**, 405–409 (1988).

9. T. C. Halsey, M. H. Jensen, L. P. Kadanoff, I. Procaccia, B. I. Shraiman, Fractal measures and their singularities: The characterization of strange sets. *Phys. Rev. A* **33**, 1141–1151 (1986).
10. T. C. Halsey, M. H. Jensen, L. P. Kadanoff, I. Procaccia, B. I. Shraiman, Erratum: Fractal measures and their singularities: The characterization of strange sets [Phys. Rev. A 33, 1141 (1986)]. *Phys. Rev. A* **34**, 1601 (1986).
11. A. L. Barabási, H. E. Stanley, *Fractal Concepts in Surface Growth* (Cambridge University Press, New York, NY, 2009).
12. P. C. Ivanov *et al*., Multifractality in human heartbeat dynamics. *Nature* **399**, 461–465 (1999).
13. L. Seuront, H. E. Stanley, Anomalous diffusion and multifractality enhance mating encounters in the ocean. *Proc. Natl. Acad. Sci. U.S.A.* **111**, 2206–2211 (2014).
14. A. Klopper, Multifractal mating. *Nat. Phys.* **10**, 183 (2014).
15. R. Deidda, Rainfall downscaling in a space–time multifractal framework. *Water Res. Res.* **36**, 1779–1794 (2000).
16. J. Alvarez-Ramirez, J. Alvarez, E. Rodriguez, Short-term predictability of crude oil markets: A detrended fluctuation analysis approach. *Energy Econ.* **30**, 2645–2656 (2008).
17. J. A. Mydosh, *Spin Glasses: An Experimental Introduction* (Taylor and Francis, London, UK, 1993).
18. P. Charbonneau *et al*., *Spin Glass Theory and Far Beyond* (World Scientific, 2023).
19. H. E. Castillo, C. Chamon, L. F. Cugliandolo, J. L. Iguain, M. P. Kennett, Spatially heterogeneous ages in glassy systems. *Phys. Rev. B* **68**, 134442 (2003).
20. E. Vincent, J. Hammann, M. Ocio, J. P. Bouchaud, L. F. Cugliandolo, "Slow dynamics and aging in spin glasses" in *Complex Behavior of Glassy Systems, Lecture Notes in Physics*, M. Rubí, C. Pérez-Vicente, Eds. (Springer, 1997), No. 492.
21. Q. Zhai, V. Martin-Mayor, D. L. Schlagel, G. G. Kenning, R. L. Orbach, Slowing down of spin glass correlation length growth: Simulations meet experiments. *Phys. Rev. B* **100**, 094202 (2019).
22. Q. Zhai *et al*., Scaling law describes the spin-glass response in theory, experiments, and simulations. *Phys. Rev. Lett.* **125**, 237202 (2020).
23. I. Paga *et al*., Spin-glass dynamics in the presence of a magnetic field: Exploration of microscopic properties. *J. Stat. Mech.: Theory Exp.* **2021**, 033301 (2021).
24. Q. Zhai, R. L. Orbach, D. L. Schlagel, Evidence for temperature chaos in spin glasses. *Phys. Rev. B* **105**, 014434 (2022).
25. F. Belletti *et al*., Simulating spin systems on IANUS, an FPGA-based computer. *Comp. Phys. Comm.* **178**, 208–216 (2008).
26. M. Baity-Jesi *et al*., A statics–dynamics equivalence through the fluctuation–dissipation ratio provides a window into the spin-glass phase from nonequilibrium measurements. *Proc. Natl. Acad. Sci. U.S.A.* **114**, 1838–1843 (2017).
27. M. Baity-Jesi *et al*., Aging rate of spin glasses from simulations matches experiments. *Phys. Rev. Lett.* **120**, 267203 (2018).
28. M. Baity-Jesi *et al*., Memory and rejuvenation effects in spin glasses are governed by more than one length scale. *Nat. Phys.* **19**, 978–985 (2023).
29. K. Jonason, E. Vincent, J. Hammann, J. P. Bouchaud, P. Nordblad, Memory and chaos effects in spin glasses. *Phys. Rev. Lett.* **81**, 3243–3246 (1998).
30. M. Baity-Jesi *et al*., Temperature chaos is present in off-equilibrium spin-glass dynamics. *Commun. Phys.* **4**, 74 (2021).
31. M. Baity-Jesi *et al*., Janus II: A new generation application-driven computer for spin-system simulations. *Comput. Phys. Commun.* **185**, 550–559 (2014).
32. M. Baity-Jesi *et al*., Critical parameters of the three-dimensional Ising spin glass. *Phys. Rev. B* **88**, 224416 (2013).
33. A. W. W. Ludwig, Infinite hierarchies of exponents in a diluted ferromagnet and their interpretation. *Nucl. Phys. B* **330**, 639–680 (1990).
34. T. Davis, J. Cardy, Correlated correlation functions in random-bond ferromagnets. *Nucl. Phys. B* **570**, 713–725 (2000).
35. E. Marinari *et al*., Multiscaling in the 3D critical site-diluted Ising ferromagnet. arXiv [Preprint] (2023). https://doi.org/10.48550/arXiv.2309.06752 (Accessed 10 September 2023).
36. W. L. McMillan, Monte Carlo simulation of the two-dimensional random ($\pm j$) Ising model. *Phys. Rev. B* **28**, 5216–5220 (1983).
37. A. J. Bray, M. A. Moore, Replica-symmetry breaking in spin-glass theories. *Phys. Rev. Lett.* **41**, 1068–1072 (1978).
38. D. S. Fisher, D. A. Huse, Ordered phase of short-range Ising spin-glasses. *Phys. Rev. Lett.* **56**, 1601 (1986).
39. R. Benzi *et al*., Extended self-similarity in turbulent flows. *Phys. Rev. E* **48**, R29–R32 (1993).
40. J. H. Chen, T. C. Lubensky, Mean field and ϵ-expansion study of spin glasses. *Phys. Rev. B* **16**, 2106–2114 (1977).
41. C. De Dominicis, I. Kondor, Spin-glass field theory in the condensed phase continued to below $d = 6$. *J. Phys. A: Math. General* **22**, L743 (1989).
42. F. Belletti *et al*., Nonequilibrium spin-glass dynamics from picoseconds to one tenth of a second. *Phys. Rev. Lett.* **101**, 157201 (2008).
43. L. A. Fernández, E. Marinari, V. Martín-Mayor, G. Parisi, J. Ruiz-Lorenzo, An experiment-oriented analysis of 2D spin-glass dynamics: A twelve time-decades scaling study. *J. Phys. A: Math. Theor.* **52**, 224002 (2019).
44. M. Baity-Jesi *et al*., The three dimensional Ising spin glass in an external magnetic field: The role of the silent majority. *J. Stat. Mech.* **2014**, P05014 (2014).
45. S. Franz, M. Mézard, G. Parisi, L. Peliti, Measuring equilibrium properties in aging systems. *Phys. Rev. Lett.* **81**, 1758–1761 (1998).
46. R. Alvarez Baños *et al*., Static versus dynamic heterogeneities in the $D = 3$ Edwards–Anderson–Ising spin glass. *Phys. Rev. Lett.* **105**, 177202 (2010).
47. M. Wittmann, A. P. Young, The connection between statics and dynamics of spin glasses. *J. Stat. Mech.: Theory Exp.* **2016**, 013301 (2016).
48. S. Jensen, N. Read, A. P. Young, Nontrivial maturation metastate-average state in a one-dimensional long-range Ising spin glass: Above and below the upper critical range. *Phys. Rev. E* **104**, 034105 (2021).
49. D. J. Amit, V. Martín-Mayor, *Field Theory, the Renormalization Group and Critical Phenomena* (World Scientific, Singapore, ed. 3, 2005).
50. D. Yllanes, "Rugged free-energy landscapes in disordered spin systems," PhD thesis, Universidad Complutense de Madrid (2011).
51. F. Belletti *et al*., An in-depth look at the microscopic dynamics of Ising spin glasses at fixed temperature. *J. Stat. Phys.* **135**, 1121 (2009).
52. P. E. Berche, C. Chatelain, B. Berche, W. Janke, Bond dilution in the 3D Ising model: A Monte Carlo study. *Eur. Phys. J. B: Condens. Matter Complex Syst.* **38**, 463–474 (2004).
53. M. Baity-Jesi *et al.*, Repository GitHub for the data and script to generate the figures in the main text. GitHub. https://github.com/JanusCollaboration/multifractal_EA/tree/main/MAIN. Deposited 12 December 2023.
54. M. Baity-Jesi *et al.*, Repository GitHub for the data and script to generate the figures in the Supporting Information. GitHub. https://github.com/JanusCollaboration/multifractal_EA/tree/main/SI. Deposited 12 December 2023.